



## Research Article

<https://doi.org/10.1631/jzus.A2500351>

# Sediment transport characteristics and siltation reduction method of high-pile wharves: a physical model and field observation study

Haojun YANG<sup>1,2</sup>, Yangyang GAO<sup>1,3</sup>✉, Lizhong WANG<sup>1,3</sup>

<sup>1</sup>Ocean College, Zhejiang University, Hangzhou 310058, China

<sup>2</sup>School of Architectural Engineering, Taizhou Vocational & Technical College, Taizhou, 318000, China

<sup>3</sup>Hainan Institute, Zhejiang University, Sanya 572025, China

**Abstract:** Siltation around high-pile wharves poses a serious threat to their structural integrity and operational safety. This study investigates tidal hydrodynamic characteristics and sediment transport patterns behind high-pile wharves through field observations and large-scale physical model experiments, providing field-supported evidence of groynes' potential to reduce sediment deposition behind the high-pile wharves. The results indicate that enhanced turbulence induced by both pile groups and sloping topography inhibits sediment deposition, while flow reduction caused by piles promotes it, with these counteracting effects jointly dominating sediment transport dynamics around the wharves. During initial tidal stages, cross-shore currents exclusively dominate sediment delivery behind the wharves. In mid-to-late stages, topography-induced alongshore currents and secondary flows regulate spatial-temporal sediment redistribution. Additionally, during the beginning and end of the tidal cycle, the extremely shallow water stage, characterized by steep velocity gradients and high shear stress, plays a significant role in driving bed changes. Physical model experiments and field data demonstrate that groynes enhance lateral flow and turbulence, thereby significantly reducing siltation behind the wharves. This study contributes to a comprehensive understanding of sediment dynamics around high-pile wharves and proposes an environmentally friendly strategy for reducing sediment deposition.

**Key words:** High-pile wharves; Field observation; Sediment transport; Large-scale physical model experiment; Groynes

## 1 Introduction

Ports play an important socioeconomic role worldwide (Chen et al., 2018; Wang et al., 2023). High-pile wharves are widely used because of their adaptability to soft seabeds and low wave loads. However, siltation behind these wharves has intensified in recent years (Zuo et al., 2019). In addition, regular dredging in front of the wharves to accommodate large vessels creates a significant elevation difference across the wharf, which may threaten pile safety (Fig. 1). Therefore, understanding the mechanisms of siltation and developing efficient, environmentally friendly mitigation measures are essential.

The morphological evolution around coastal

structures, encompassing both sedimentation and erosion processes, results from complex nonlinear interactions among hydrodynamics, shoreline dynamics, subsurface soil dynamics (e.g., pore-pressure response and effective-stress evolution), and human activities across multiple temporal and spatial scales (Hapke et al., 2013; Stive et al., 2002; Hu and Li, 2025; Hu et al., 2025). Previous studies have shown that turbulence plays a key role in sediment transport by enhancing erosion (Li et al., 2018), altering suspended sediment distribution (Luo et al., 2022), and inducing seabed scour around pile groups (Yang et al., 2020; Zhang et al., 2023). These findings suggest that the balance between flow deceleration and turbulence enhancement governs morphological evolution around wharves. However, the underlying mechanisms remain insufficiently understood. Many high-pile wharves are located in regions with dense islands and irregular shorelines, where complex topography generates large-scale flow fields that strongly affect sediment transport. Existing studies mainly rely on small-scale flume experiments

✉ Yangyang GAO, yygao@zju.edu.cn

Haojun YANG, <https://orcid.org/0000-0001-7069-3728>

Received July 26, 2025; Revision accepted Apr. 8, 2026;  
Crosschecked

or short-term numerical simulations (Ma et al., 2018; Schendel et al., 2018; Whitehouse et al., 2023; Wang et al., 2024), limiting the understanding of sediment dynamics under such conditions. In addition, flood–ebb asymmetry can accumulate over multiple tidal cycles, causing significant temporal variations in sediment transport. Long-term investigations remain scarce, leading to continued uncertainty in sediment transport and morphological evolution around high-pile wharves.

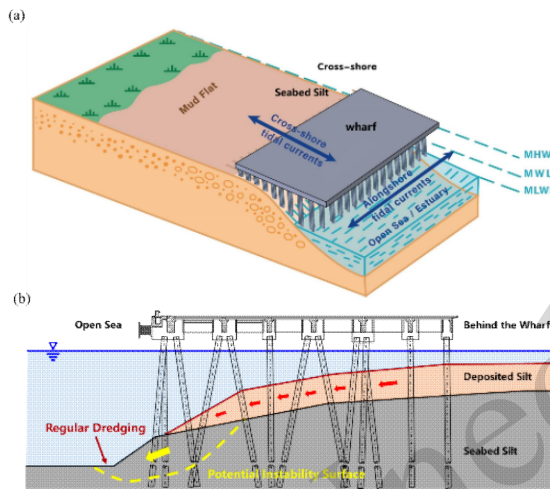


**Fig. 1** (a) Sketch of a high-pile wharves morphology influenced by cross-shore and alongshore tidal currents (MHWL, MWL, and MLWL represent mean high-water level, mean water level, and mean low-water level, respectively), modified from Wang et al. (2019), (b) mechanism of disaster caused by siltation at a high-pile wharves (profile view)

Groynes are widely used in coastal engineering for flow regulation and sediment control. Previous studies have shown that they can modify current structures, increase local flow velocity, reduce sediment deposition, and enhance sediment transport (Alvarez et al., 2021; Liu et al., 2022; Zhou et al., 2024). However, the areas behind high-piled wharves are semienclosed, and their hydrodynamic and sediment transport processes, influenced by tides, topography, and pile structures, differ markedly from those on open coasts. Owing to the lack of field observations and engineering validation, it remains unclear whether the sediment reduction mechanisms of groynes identified in coastal environments are directly applicable to high-piled wharf regions.

## 2. Study Area

The study area is located on the Chuanshan Peninsula in Ningbo, between Hangzhou Bay and the East China Sea (Fig. 2). The tidal regime features an asymmetric semidiurnal pattern (Chu et al., 2021) with a mean tidal range of 2.5 m. Tidal currents flow east–southeast (ESE) during flood tide and west–northwest (WNW) during ebb tide, aligning parallel to depth contours (Figs. 2c, d). Sediment primarily originates from the Yangtze River-derived suspended load transported via Hangzhou Bay. The suspended particles are very fine, with a median particle size of 0.01 mm in the wharve area (Fig. 2(e)). Over the past 21 years, sedimentation behind the wharves has accumulated at 10 m height, causing the mudflat to be exposed at low tide (Fig. 2f), while the high tide water depth reaches 2.3 m.

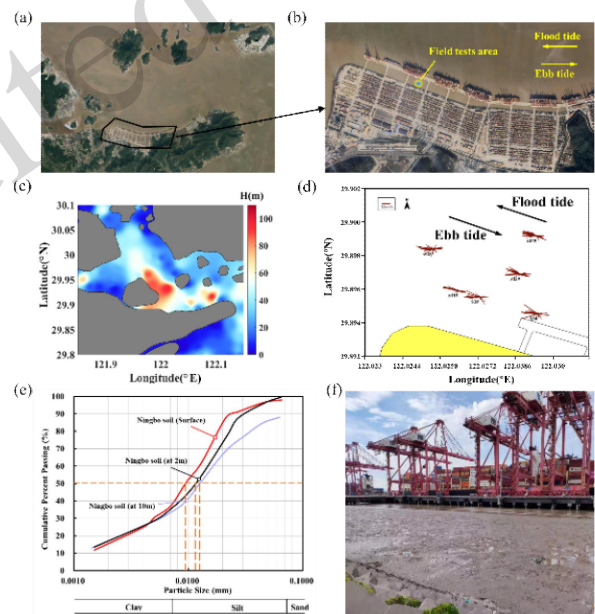


**Fig. 2.** Details of the present study area: (a) and (b) study area location; (c) water depth contours; (d) vector graph of flow velocity in the study area in November 2021; (e) size distribution; (f) field experiment site (behind the 3# wharf) during low tide

## 3 Methodology

### 3.1 Field observation and experiments

In November 2021, tidal levels and flow velocities in front of the wharf were measured at six temporary stations (A–F; Fig. 3(a)) using a Nortek AWAC and a 1,200-kHz ADCP. Behind the wharf, topography and flow velocity were surveyed using an HD-MAX echo sounder and a shipboard ADCP.

Additional velocity and topographic surveys were conducted in 2020 and 2022 (Fig. 3(b)–(e)). From September 29 to October 3, 2022, a tripod equipped with a wave-tide recorder, OBS-3A, and ADV was deployed behind the wharf to monitor eight tidal cycles and quantify intratidal hydrodynamic and erosion-deposition processes (Fig. 4). The ADV sampled at 16 Hz, while shallow-water velocity (<0.2 m) was measured using an EMCM at 2 Hz; bed elevation and exposed topography were recorded by the ADV and a total station, respectively.

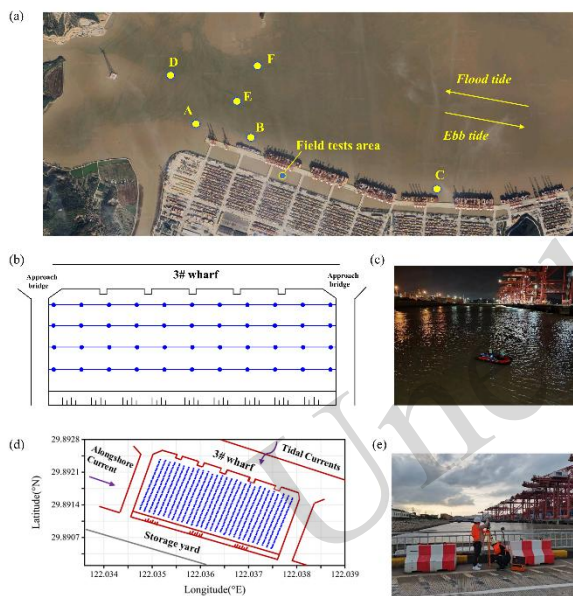


**Fig. 3 Schematic drawing of observed stations and points (tidal, flow velocity and topography). (a) observed stations front the wharf; (b) configuration of flow velocity measured points behind the 3# wharf; (c) flow velocity measurement using ADCP; (d) configuration of topography measured points behind the 3# wharf; (e) RTK topography observation**

Field measurements of flow velocity and topography using ADV and EMCM are reliable and have been widely used in field studies (Shi et al., 2019; Ton et al., 2023), with detailed processing and validation provided in Section S4 of the ESM. OBS-3A, installed 0.05 m above the bed and sampling at 1 Hz, was used to estimate the suspended sediment concentration (SSC) through calibration with field water samples. The bed shear stress was calculated from field-derived hydrodynamic parameters (the calculation formula is provided in Section S5 of the electronic supplementary materials

(ESM)).

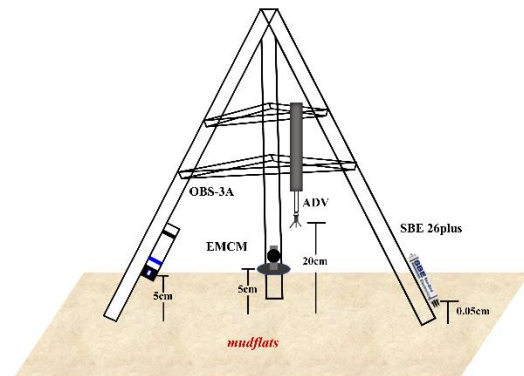


**Fig. 4 Schematic diagram of the tripod and instruments deployed at the observation location**

The groyne was installed behind the wharf, perpendicular to the shoreline, on November 19, 2022. Fig. 5 presents a schematic diagram of the groyne layout. The groyne is 20 meters long, 2.6 meters wide, and 2.3 meters high and is secured to the seabed with six mooring chains. It remains in constant contact with the seabed surface, without floating or moving laterally, and stays unsubmerged. To evaluate its sediment-reduction efficacy, six topographic surveys were conducted from 2022 to 2023 using the same device arrangements and measurement points described in Section 3.1.

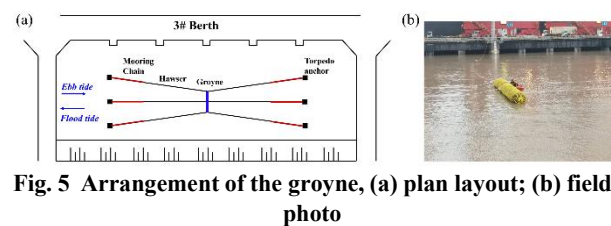


**Fig. 5 Arrangement of the groyne, (a) plan layout; (b) field photo**

### 3.2 Physical model experiment

Large-scale physical model experiments were conducted in a wave-current basin at the Coastal Laboratory, Ocean College, Zhejiang University (70 m × 40 m × 1.5 m; Fig. 6). The experimental design ensured similarity in hydrodynamics and sediment transport between the model and prototype. For any characteristic parameter  $\Phi$ , its scale ratio is defined as Eq. (1)

$$\lambda_{\phi} = \frac{\Phi_p}{\Phi_m} \quad (1)$$

where p and m denote the prototype and model, respectively. Considering the basin conditions, the horizontal geometric scale ratio was set to 150 to enlarge the coverage area and reduce boundary effects. A distorted model with a separate water-depth scale ratio was adopted to minimize shallow-water effects (Huang et al., 2020). All scale ratios are listed in Table 1, with the derivation and validation of the relevant formulas given in Sections S1 and S2 of the electronic supplementary material.

**Table 1 Details of model scale ratio values for the present experiment**

Model scale ratio	Symbol	Theoretical value	Corrected value
Horizontal geometric scale	$\lambda_1$	150	
Water depth scale	$\lambda_h$	50	
Flow time scale	$\lambda_{t_1}$	21.21	
Velocity scale	$\lambda_u$	7.07	
Roughness scale	$\lambda_n$	1.11	
Sediment settlement velocity scale	$\lambda_w$	2.36	2.29
Sediment initiation velocity scale	$\lambda_{u_c}$	7.07	6.32
Sediment content scale	$\lambda_s$	0.27	
Sediment transport time scale	$\lambda_{t_2}$	118.44	156

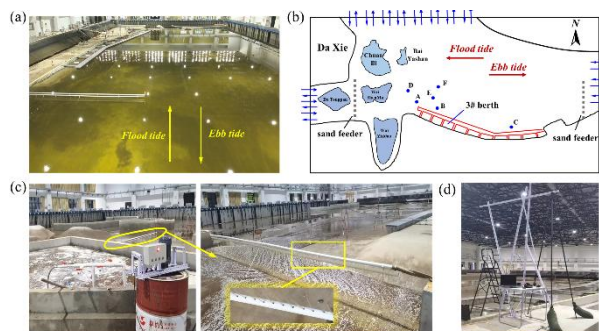


**Fig.6 Experimental layout diagram, (a) experiment setup photo; (b) plan view; (c) sand feeder device; (d) surface flow field observed device (LSPIV)**

## 4 Results and discussion

### 4.1 Large-scale plane flow field characteristics

The present study investigates the interaction between topography and flow fields, examining their impact on sediment transport around the high-pile wharf at Zhoushan Port, which serves as the study area. The study area contains numerous islands and intersecting waterways, and large-scale planar flow characteristics are explored during flood and ebb tides using the flow visualization method. This approach enables the identification of large-scale flow structures at the free surface. A similar method is employed by Jeon et al. (2018) to visualize the free surface flow structure.

Figs. 7 and 8 illustrate the main current movement trends in the study area during the flood and ebb tides, respectively. As shown in Fig. 11, the flood tide in the large-scale flow field splits into two branches due to the topography of the Chuanshan Peninsula. Due to shoreline topographic changes, the alongshore current forms a counterclockwise recirculation zone at the wharf corner, resulting in a reverse flow around the wharf during flood tide that opposes the main current. The other branch of the flood tide mainstream continues westward. Near Wai Shenma Island, this current further divides into two distinct branches: the western branch flows through the Chuanshan Channel, while the other branch merges into the Luotou Channel east of Chaibishan Island.

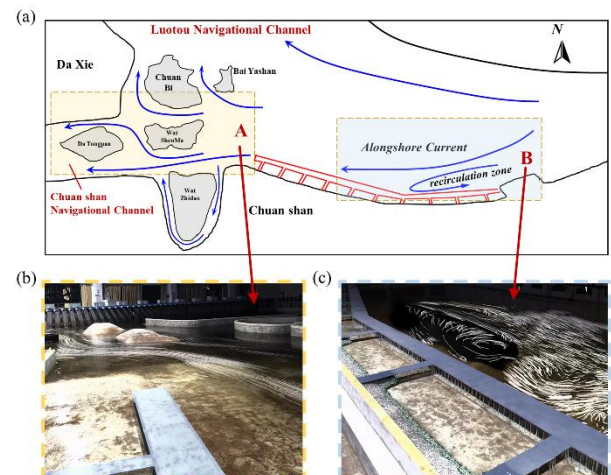


**Fig. 7 Flow pattern during flood tide in the study area; (a) overall flow pattern; (b) flow visualization in area A; (c) flow visualization in area B**

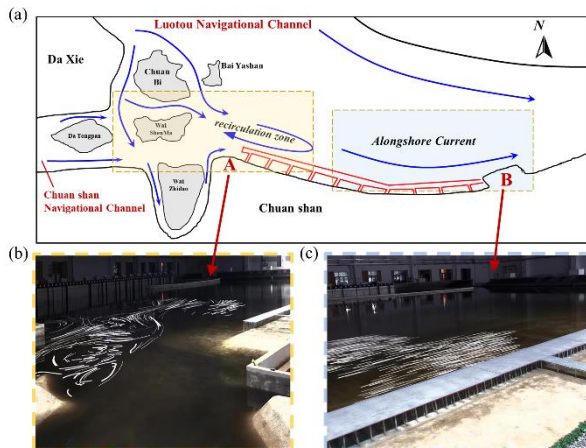
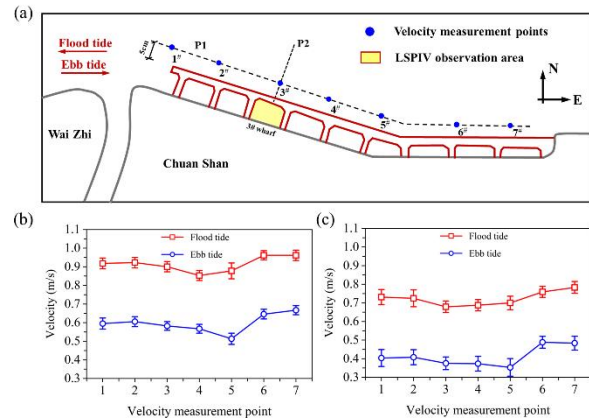


**Fig. 8** Flow patterns in the study area during ebb tide; (a) overall flow pattern; (b) flow visualization in area A; (c) flow visualization in area B

As shown in Fig. 8, during the ebb tide, the currents predominantly enter the study area through the Luotou and Chuanshan channels. The presence of islands, such as Daxie and Wai shenma, induces a deflection in the current, resulting in a significant clockwise recirculation zone west of the wharf. This recirculation is primarily attributed to two factors: vortex shedding in the wake of the islands and the sudden expansion of the flow area, which contribute to a reverse flow relative to the main current direction on the west side of the wharf during the ebb tide. This deflection effect becomes more pronounced during the peak of the ebb tide and is further enhanced by the flood tide entering the Luotou Waterway.

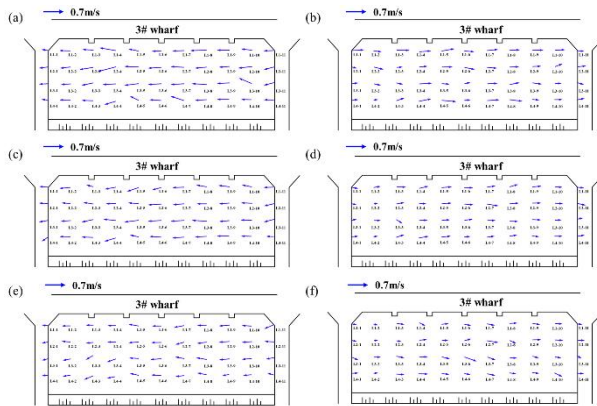
#### 4.2 Small-scale flow field around the wharf

To investigate the influence of small-scale flow patterns around the wharf on topographic evolution, seven flow velocity measurement points (P1 transect) are positioned parallel to the front of the wharf in a large physical model. A propeller current meter is used to measure flow velocity over six consecutive tidal cycles during both spring and neap tidal periods. Due to the shallow water depth behind the wharf, large-scale particle image velocimetry (LSPIV) is utilized to measure the velocity to avoid measurement errors caused by the propeller current meter. The configuration of the measurement points is shown in Fig. 9.



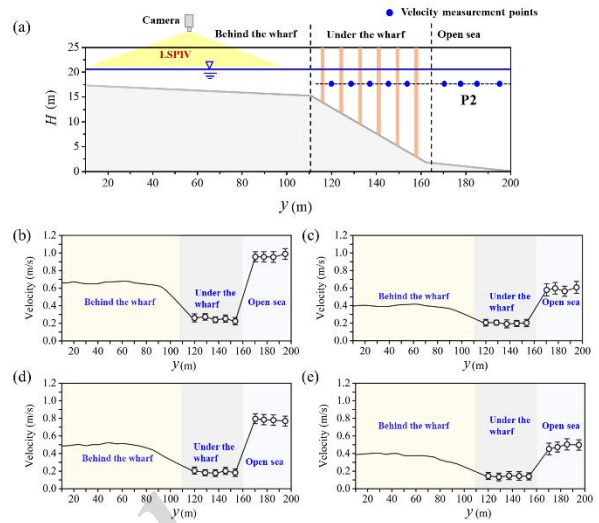
**Fig. 9** Flow velocity measurements around the wharf; (a) P1 cross-sectional measurement point layout; (b) average velocity distribution at the wharf front during spring tide; (c) average velocity distribution at the wharf front during neap tide. Error bars indicate  $\pm$ one standard deviation in spatially-averaged velocity values

To reduce experimental uncertainty, the flow velocity in front of the wharf was measured six times, and the mean and standard deviation ( $\sigma$ ) were calculated. As shown in Figs. 9(b) and 9(c), the velocity is higher during flood tide than ebb tide and higher during spring tides than neap tides, with a flood tide velocity approximately 1.6 times that of ebb tide. The velocity is generally greater east of the wharf, indicating stronger sediment transport capacity there, while lower velocities at points 4# and 5#, caused by a recirculation zone near the wharf corner, favor sediment deposition. The higher turbulence intensity at points 5# - 7# results from the interaction between large-scale recirculation and the shear layer induced by the pile groups, which enhances offshore sediment entrainment into the wharf region. Fig. 10 shows the depth-averaged flow velocity behind Wharf #3. The velocity is also higher during flood tide than ebb tide and decreases from spring tide to neap tide. In addition to the primary alongshore tidal current, a secondary shoreward flow is observed, mainly driven by the large-scale recirculation induced by the surrounding topography, gravity effects over the sloping bed, and the water-level gradient caused by the depth difference between the front and rear of the wharf.



**Fig. 10** Measured vertical average flow velocity vectors behind 3# wharf (the numbers indicate the flow-velocity measurement station numbers): (a) spring tide flood; (b) spring tide ebb; (c) mid-tide flood; (d) mid-tide ebb; (e) neap tide flood; (f) neap tide ebb

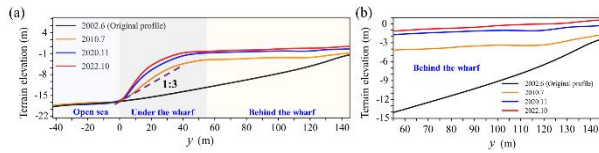
Fig. 11 shows the current velocity distribution along the longitudinal profile (P2) at the wharf centerline in the large-scale physical model, with the measurement layout given in Fig. 11(a). Flow velocities behind Wharf #3 were obtained using LSPIV, and the solid gray line denotes the bed profile based on field elevation data. The water depth ratio between the front and rear of the wharf is  $rh = 8$ , indicating shallow-flow conditions ( $rh > 3$ ) characterized by monotonic velocity profiles and a marked velocity gradient across the sloping region. In this study, the flow velocity in front of the wharf is approximately 1.4 times that behind it, lower than the value of 1.75 reported by Stocchino and Brocchini (2010). This is mainly because the pile groups beneath the wharf suppress secondary currents and cross-shore transport. Although the front-rear velocity gradient enhances shear and sediment transport in the sloping region, the pile groups substantially reduce the flow velocity beneath the wharf, leading to a much lower sediment transport capacity there. As a result, sediment transported by tidal currents tends to accumulate within the pile-group region, forming the main deposition area.



**Fig. 11** Velocity distribution around the wharf ( $y$ -direction); (a) distribution of measured velocity points along the P2 profile and LSPIV measurement zone behind the wharf; (b) spring tide flood velocity; (c) spring tide ebb velocity; (d) neap tide flood velocity; (e) neap tide ebb velocity. Error bars indicate  $\pm$  one standard deviation in spatially-averaged velocity values

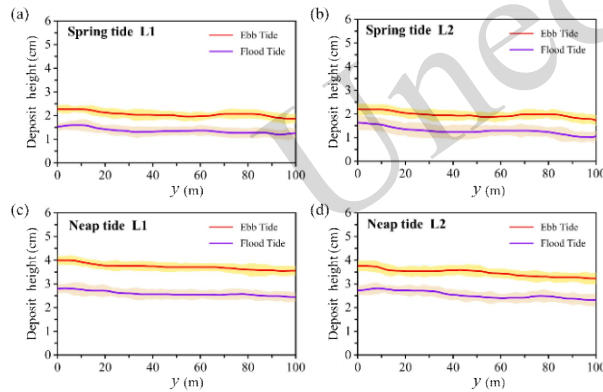
### 4.3 Wharf topography evolution

Fig. 12 shows the evolution of the central cross-sectional topography of Wharf #3 based on field measurements. Owing to the sheltering effect of the pile groups, the flow velocity beneath the wharf decreases, reducing the sediment transport capacity and promoting continuous deposition. Rapid initial accumulation forms a steep slope, which developed quickly after construction and became evident by 2010. As the slope steepens, gravity-driven redistribution, together with enhanced bed shear stress and turbulence, promotes sediment resuspension and transport, thereby reducing the net deposition flux and slowing seabed aggradation beneath the wharf. In contrast, the relatively uniform flow field behind the wharf (Fig. 11) results in a more uniform topography. As sediment gradually accumulates there, the water depth decreases, shortening the deposition duration within each tidal cycle and causing the annual siltation rate to progressively decline after the initial rapid stage.



**Fig. 12 Topography elevation of the central cross-section at the 3# wharf. (a) elevation of the overall profile at the 3# wharf; (b) elevation of the profile behind the 3# wharf**

To further investigate the primary evolution process and pattern of sediment deposition behind the wharf during tidal cycles, the sediment deposition height was measured in the physical model experiments during both flood and ebb tides. The experimental results are presented in Fig. 13. The variation in bed elevation is defined as the difference in bed elevation between two consecutive ebb and flood tides. The bed elevation data are obtained using a resistive depth gauge. To minimize the measurement errors, the topographical data measured over six tidal cycles are statistically averaged.



**Fig. 13 Bed elevation changes during spring and neap tides behind the 3# wharf. (a) changes in bed elevation at measure line L1 during spring tide; (b) changes in bed elevation at measure line L2 during spring tide; (c) changes in bed elevation at measure line L1 during neap tide; (d) changes in bed elevation at measure line L2 during neap tide. The solid line is the mean deposit height and the bar is the standard deviation of the six tidal cycle statistics**

Fig. 13 illustrates that sediment deposition during spring tides is generally lower than that during neap tides, while deposition during ebb tides is significantly greater than that during flood tides. This pattern can be attributed to the reduced flow velocity during neap and ebb tides, which weakens sediment suspension capacity and increases the deposition flux.

As a result, sediment accumulation behind the wharf predominantly occurs during the neap and ebb tide phases. This uniformity in flow velocity facilitates stable sediment transport, contributing to a more homogeneous deposition pattern.

Fig. 14 presents field-measured temporal variations in the near-bed suspended sediment concentration and seabed topographic evolution at a specific location behind Wharf #3. Bed-level changes are represented by variations in the distance between the bed and the ADV probe. During the eight tidal cycles, the maximum significant wave height is 0.23 m. According to the formula proposed by Nielsen (1992), the thickness of the wave-induced bottom boundary layer is estimated to be less than 1 cm; therefore, wave effects can be neglected in this study. As shown in Fig. 14(d), the main erosion phase occurs during the flood tide, whereas deposition is dominated by the ebb tide.

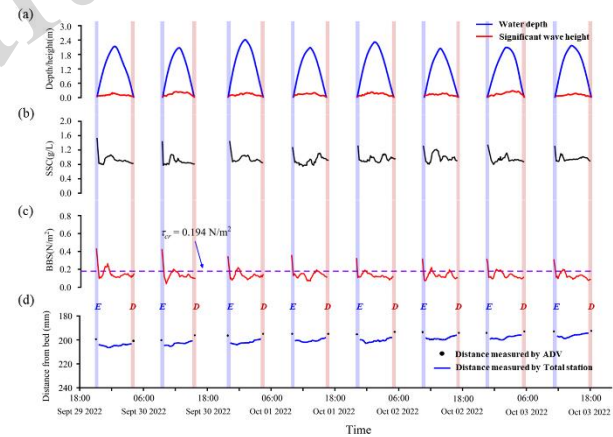


**Fig.14 Time-series of (a) water depth and significant wave height, (b) suspended sediment concentration (SSC), (c) bed shear stress (BBS), and (d) bed-level changes. The extremely shallow water stages (ESWS) during flood and ebb tides are marked with color bars. Blue bars indicate erosional phases in the flood tide stage (denoted by E) and red bars indicate depositional phases at the ebb tide stage (denoted by D)**

The topographic evolution around high-pile wharves is illustrated in Fig. 15. During the early flood tide, rising water levels generate a cross-shore current in addition to the dominant alongshore current, transporting sediment from the shoreline to the area behind the wharf, where part of it is deposited beneath the pile groups. During the early ebb tide, sediment is transported toward the wharf front, while

some is still retained beneath the wharf due to the sheltering effect of the piles. This cross-shore transport is strongest in the early stages of both flood and ebb tides, leading to marked deposition beneath the wharf and a relatively flat bed behind it. After submergence of the wharf area, the alongshore current becomes dominant and induces a secondary current in the shallow zone toward the wharf front, further promoting sediment transport. Overall, sediment transport over a tidal cycle is mainly controlled by the alongshore current and its induced secondary flow, which together shape the seabed topography around high-pile wharves.

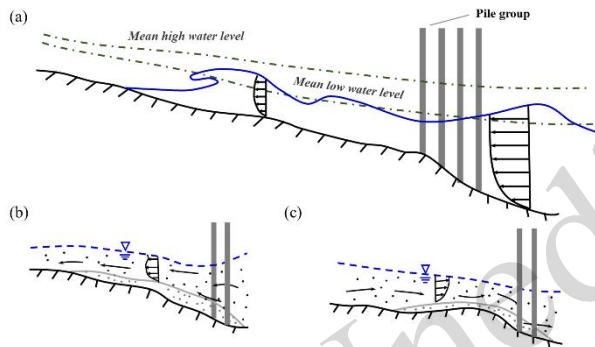


**Fig. 15** Sedimentation dynamics processes at the high-pile wharves; (a) hydrodynamic pattern of the wharf cross-section (as an example of spring tide); (b) sediment transport pattern during flood tide; (c) sediment transport pattern during ebb tide

#### 4.4 Effects of groynes on sedimentation behind high-pile wharves

In this study, a groyne was deployed behind the wharf to regulate flow and reduce sedimentation. Compared with the case without a groyne (Fig. 10), Fig. 16 shows that the groyne clearly deflects the flow during both ebb and flood tides, altering the velocity distribution and sediment transport on both sides. Eddy activity near the groyne enhances fluid mixing, bottom shear stress, and local sediment resuspension, while the redistribution of the main and secondary flows and the formation of a wake stagnation point indicate that the groyne strengthens lateral flow, improves hydrodynamic conditions, and optimizes sediment distribution behind the wharf.

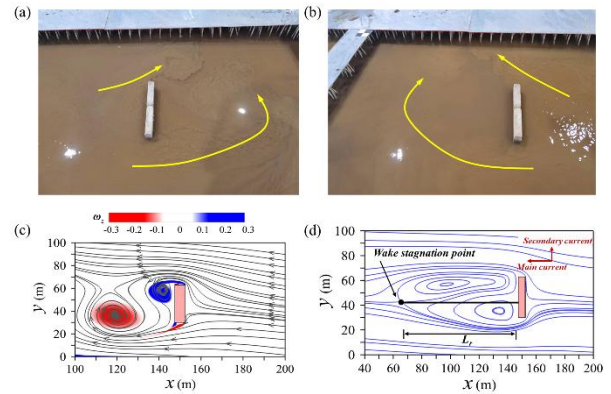


**Fig. 16** Patterns of high-sediment-content movement around groyne, (a) ebb tide; (b) flood tide; (c) streamlines of the instantaneous flow and vertical vorticity field; (d) streamlines of mean flow

Different groyne lengths and layout angles ( $\theta$ ) were examined in the physical model. The groyne length  $L$  was normalized by the width  $B$  of the area behind the wharf, giving the blockage ratio  $\beta=L/B$ . The case settings are listed in Table 2. Fig. 17 presents the LSPIV results of the turbulent kinetic energy, time-averaged flow velocity, and recirculation zone length under different groyne angles. The results show that the turbulent kinetic energy within the recirculation zone is highest at  $\theta=90^\circ$ , owing to enhanced eddy activity. The lateral flow velocity and Reynolds shear stress distributions further indicate stronger turbulence mixing, which promotes sediment suspension and lateral transport, particularly at  $\theta=90^\circ$ . In this case, the average flow velocity on both sides of the groyne increases to approximately 1.6 times the normal flow velocity, effectively reducing downstream siltation. Although the recirculation zone has a relatively low mean velocity, the combined increase in lateral velocity and Reynolds shear stress enhances sediment resuspension and transport, offsetting potential deposition. In addition, the recirculation zone length at  $\theta=90^\circ$  is approximately twice the groyne length, enlarging the flow–sediment interaction area and further improving sediment transport capacity.

**Table 2** Table 2. Details of different cases for the deployment of groyne

Case	Blockage ratio ( $\beta$ )	Groyne arrangement angle ( $\theta$ )	Reduction in mean deposition depth (%)

1	1/5	45°	6.2%
2	1/5	90°	7.7%
3	1/5	135°	4.3%
4	1/3	45°	11.4%
5	1/3	90°	15.7%
6	1/3	135°	14.8%
7	1/2	45°	22.1%
8	1/2	90°	22.5%
9	1/2	135°	24.6%

sediment is entrained into the recirculation zone behind the groyne by the mixing layer.

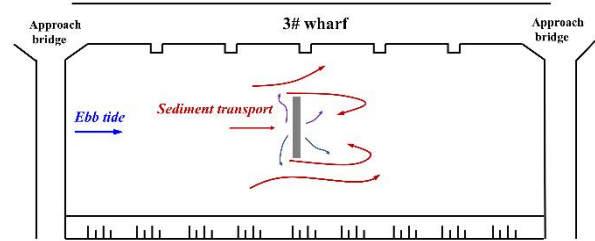


**Fig. 18.** The sediment transport trends behind the wharf during ebb tide with groyne configurations. The red lines represent four main sediment transport patterns, while the purple lines denote the movement patterns of sediment resuspension after deposition

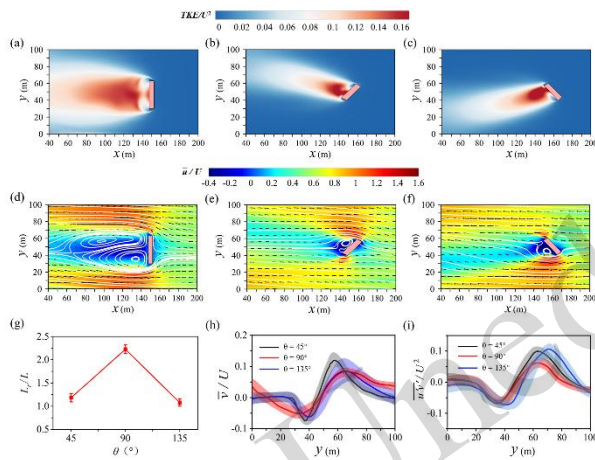


**Fig. 17.** Flow characteristics of groyne with different layout forms. (a) – (c) dimensionless turbulent kinetic energy ( $TKE/U^2$ ) at  $\theta = 90^\circ, 45^\circ, 135^\circ$ ; (d) – (f) dimensionless time-averaged flow velocities ( $\bar{u}/U$ ) at  $\theta = 90^\circ, 45^\circ, 135^\circ$ ; (g) dimensionless lengths of the recirculation zones ( $L_r/L$ ) for groyne of different lengths at  $\theta = 90^\circ, 45^\circ, 135^\circ$  respectively; (h, i). dimensionless transverse flow velocities ( $\bar{v}/U$ ) and Reynolds stresses ( $\overline{u'v'}/U^2$ ) at  $x = 125m$  for  $\theta = 90^\circ, 45^\circ, 135^\circ$ , respectively.

The error bars and bands in the figure represent the standard deviation for groyne of different lengths

The characteristics of the flow field indicate that the sediment transported by the flow after passing the groyne moves in three primary directions, as shown in Fig. 18. Since the main silting process occurs during the ebb tide, the ebb tide is taken as an example for analysis. A portion of the sediment continues to be transported downstream along the main flow parallel to the shoreline. Some sediment is deposited due to the obstruction effect of the groyne. Another portion is transported toward the front of the wharf under the deflection effect of the groyne. The remaining

Based on the physical model experiments, Fig. 19 shows that the groyne effectively reduces sediment accumulation behind the wharf and redistributes the deposition pattern. Deposition mainly occurs on the right side of the groyne during ebb tide, when sediment is transported into the low-velocity recirculation zone and settles, while sediment near the wharf is trapped by the diverted flow and pile groups. In contrast, the asymmetric scour pits indicate that erosion mainly occurs during flood tide under higher and longer-lasting velocities. Overall, the ebb tide is dominated by suspended sediment transport that initiates deposition, whereas the flood tide is dominated by bedload transport that reshapes the deposited sediment. Fig. 20 shows that groyne deployment effectively reduces the average sedimentation depth behind the wharf, with the reduction efficiency increasing with the groyne length and reaching 24.6% when the groyne length is approximately half the width of the rear region. The effect of the layout angle is limited, although  $\theta=90^\circ$  performs slightly better.

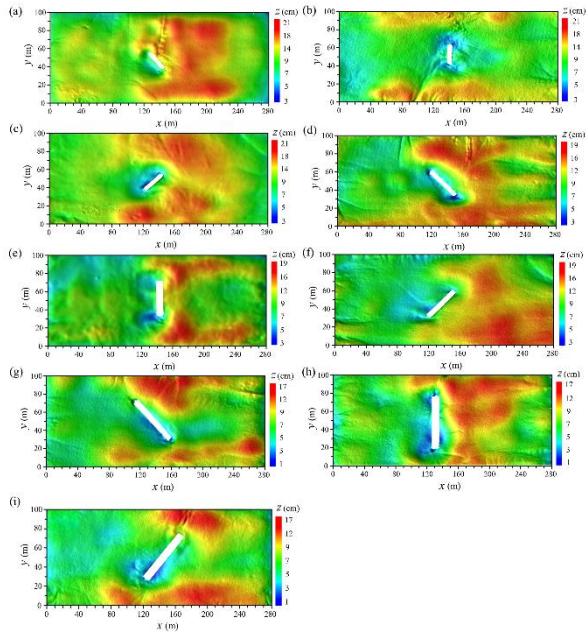


**Fig. 19** Topographic contours in the behind of the 3# wharf at different  $\beta$  and  $\theta$ : (a)–(c)  $\beta = 1/5$ ,  $\theta = 45^\circ, 90^\circ, 135^\circ$ ; (d)–(f)  $\beta = 1/3$ ,  $\theta = 45^\circ, 90^\circ, 135^\circ$ ; (g)–(i)  $\beta = 1/2$ ,  $\theta = 45^\circ, 90^\circ, 135^\circ$

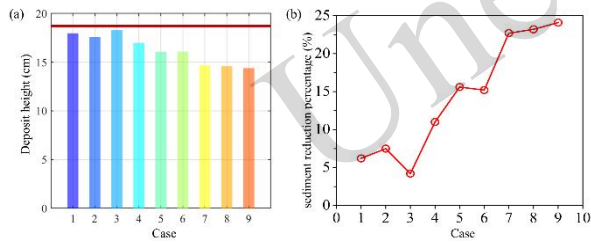


**Fig. 20** Sediment reduction efficiency of groyne for different cases

Six field topographic surveys conducted in 2023 following the groyne installation behind the wharf in November 2022 revealed a notable decrease in sediment accumulation in the rear area, as illustrated in Fig. 21. This is primarily attributed to the groyne enhancing the secondary flow directed toward the front of the wharf and generating a high-shear region. These hydrodynamic changes increase the sediment-carrying capacity of the flow, promote sediment transport toward the wharf front, and consequently reduce deposition behind the wharf.

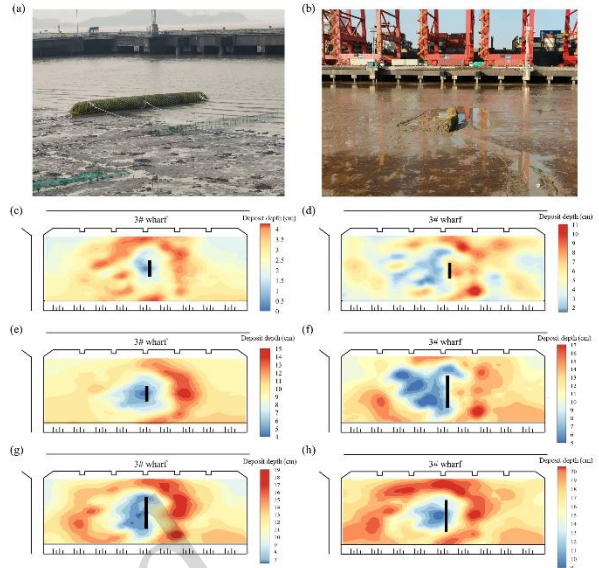


**Fig. 21** Evolution of sedimentation height behind the 3# wharf, (a)–(b) field layout of groyne; (c) December 21, 2022; (d) March 7, 2023; (e) May 17, 2023; (f) July 6, 2023; (g) September 28, 2023; and (h) November 19, 2023

## 5 Conclusions

A series of field observations and large-scale physical model experiments were conducted to investigate sediment transport and siltation mechanisms behind high-pile wharves, as well as the feasibility of groynes for siltation reduction. The main conclusions are as follows:

(1) Complex topography regulates the large-scale flow field around high-pile wharves and thus controls sediment transport. Recirculation zones induced by islands and irregular shorelines promote sediment deposition near the wharf, while reverse flows weaken the scouring effect of the mainstream.

(2) Sediment transport and topographic evolution behind the wharf are strongly controlled by tidal cycles. Early flood and ebb stages are dominated by cross-shore transport, whereas alongshore and secondary flows become dominant after submergence. During tidal transitions, shallow water, high shear stress, and sharp velocity gradients intensify sediment entrainment.

(3) Wharf pile groups reduce flow velocity and promote sediment deposition, while slope topography further regulates transport patterns. Under gentle slopes, weak turbulence cannot offset deposition, whereas steeper slopes enhance turbulence and

gradually establish a balance between deposition and resuspension.

(4) Groyne deployment enhances turbulent kinetic energy and deflected flow, strengthening cross-shore sediment transport and increasing local scouring through coherent structures on both sides. A one-year field survey further confirms that groynes can effectively mitigate sedimentation behind the wharf. stress, leading to significant scouring. Additionally, a year-long field survey demonstrates that groynes effectively mitigate sedimentation behind the wharf.

### Acknowledgments

This research was supported by Key Research and Development Program of Zhejiang Province (Grant No. 2021C03014).

### Author contributions

Lizhong WANG designed the research. Haojun YANG processed the corresponding data and wrote the first draft of the manuscript. Yangyang GAO and Haojun YANG revised and edited the final version.

### Conflict of interest

Haojun YANG, Yangyang GAO, and Lizhong WANG declare that they have no conflict of interest.

### Data availability

The data that support the findings of this study are available from the corresponding author upon reasonable request.

### References

- Chen Y, Wei Y, Peng L, 2018. Ecological technology model and path of seaport reclamation construction. *Ocean & Coastal Management*, 165: 244-257.  
<https://doi.org/10.1016/j.ocecoaman.2018.08.031>
- Chu D, Niu H, Wang Y P, et al., 2021. Numerical study on tidal duration asymmetry and shallow-water tides within multiple islands: An example of the Zhoushan Archipelago. *Estuarine, Coastal and Shelf Science*, 262: 107576.  
<https://doi.org/10.1016/j.ecss.2021.107576>
- Hapke C J, Kratzmann M G, Himmelstoss E A, 2013. Geomorphic and human influence on large-scale coastal change. *Geomorphology*, 199: 160-170.  
<https://doi.org/10.1016/j.geomorph.2012.11.025>
- Hu Z, Li Y P, 2025. Full-scale tsunami-induced scour around a circular pile with three-dimensional seepage. *Coastal Engineering*, 197: 104676.  
<https://doi.org/10.1016/j.coastaleng.2024.104676>
- Hu Z, Qi W G, Li Y P, 2025. The role of dynamic seepage response in sediment transport and tsunami-induced scour. *Journal of Geophysical Research: Oceans*, 130(3): e2024JC021084.  
<https://doi.org/10.1029/2024JC021084>
- Huang J J, Chen G P, Yu Q, 2020. Experimental Study on Influence of Pile Wall on Flow Field Around Pile-Supported Wharf. *Journal of Waterway, Port, Coastal, and Ocean Engineering*, 146(5): 04020025.  
[https://doi.org/10.1061/\(ASCE\)WW.1943-5460.0000573](https://doi.org/10.1061/(ASCE)WW.1943-5460.0000573)
- Jeon J, Lee J Y, Kang S, 2018. Experimental investigation of three-dimensional flow structure and turbulent flow mechanisms around a nonsubmerged spur dike with a low length-to-depth ratio. *Water Resources Research*, 54(5): 3530-3556.  
<https://doi.org/10.1029/2017WR021582>
- Li Y, Wei J, Gao X, et al., 2018. Turbulent bursting and sediment resuspension in hyper-eutrophic Lake Taihu, China. *Journal of Hydrology*, 565: 581-588.  
<https://doi.org/10.1016/j.jhydrol.2018.08.067>
- Ma L, Wang L, Guo Z, et al., 2018. Time development of scour around pile groups in tidal currents. *Ocean Engineering*, 163: 400-418.  
<https://doi.org/10.1016/j.oceaneng.2018.06.035>
- Schendel A, Hildebrandt A, Goseberg N, et al., 2018. Processes and evolution of scour around a monopile induced by tidal currents. *Coastal Engineering*, 139: 65-84.  
<https://doi.org/10.1016/j.coastaleng.2018.05.004>
- Shi B, Cooper J R, Li J, et al., 2019. Hydrodynamics, erosion and accretion of intertidal mudflats in extremely shallow waters. *Journal of Hydrology*, 573: 31-39.  
<https://doi.org/10.1016/j.jhydrol.2019.03.065>
- Stive M J F, Aarninkhof S G J, Hamm L, et al., 2022. Variability of shore and shoreline evolution. *Coastal engineering*, 47(2): 211-235.  
[https://doi.org/10.1016/S0378-3839\(02\)00126-6](https://doi.org/10.1016/S0378-3839(02)00126-6)
- Stocchino A, Brocchini M, 2010. Horizontal mixing of quasi-uniform straight compound channel flows. *Journal of Fluid Mechanics*, 643: 425-435.  
<https://doi.org/10.1017/S0022112009992680>
- Sukhodolov A N, Sukhodolova T A, Krick J, 2017. Effects of vegetation on turbulent flow structure in groyne fields. *Journal of Hydraulic Research*, 55(1): 1-15.  
<https://doi.org/10.1080/00221686.2016.1211183>
- Ton A M, Vuik V, Aarninkhof S G J, 2023. Longshore sediment transport by large-scale lake circulations at low-energy, non-tidal beaches: A field and model study. *Coastal Engineering*, 180: 104268.  
<https://doi.org/10.1016/j.coastaleng.2022.104268>
- Wang N, Zhu G, Li X, et al., 2023. Transitions and suggestions for China's coastal port reclamation policies. *Ocean & Coastal Management*, 236: 106532.  
<https://doi.org/10.1016/j.ocecoaman.2023.106532>
- Wang S Y, Qi W G, Li B, et al., 2024. Tidal currents-induced

- scour development around pile foundations: Effects of flow velocity hydrograph. *Coastal Engineering*, 191: 104533.  
<https://doi.org/10.1016/j.coastaleng.2024.104533>
- Wang Y, Wang Y P, Yu Q, et al., 2019. Sand-mud tidal flat morphodynamics influenced by alongshore tidal currents. *Journal of Geophysical Research: Oceans*, 124(6): 3818-3836.  
<https://doi.org/10.1029/2018JC014550>
- Whitehouse R J S, Stroescu E I, 2023. Scour depth development at piles of different height under the action of cyclic (tidal) flow. *Coastal Engineering*, 179: 104225.  
<https://doi.org/10.1016/j.coastaleng.2022.104225>
- Yang Y, Melville B W, Macky G H, et al., 2020. Experimental study on local scour at complex bridge pier under combined waves and current. *Coastal Engineering*, 160: 103730.  
<https://doi.org/10.1016/j.coastaleng.2020.103730>
- Zhang Q, Gong Z, Zhang C, et al., 2016. Velocity and sediment surge: what do we see at times of very shallow water on intertidal mudflats? *Continental Shelf Research*, 113: 10-20.  
<https://doi.org/10.1016/j.csr.2015.12.003>
- Zhang Z, Du S, Guo Y, et al., 2023. Field study of local scour around bridge foundations on silty seabed under irregular tidal flow. *Coastal Engineering*, 185: 104382.  
<https://doi.org/10.1016/j.coastaleng.2023.104382>
- Zhou Z, Ge J, Van Maren D S, et al., 2024. Groyne-induced effects on channel-shoal exchange and saltwater intrusion in estuarine environments. *Journal of Hydraulic Engineering*, 150(1): 04023056.  
<https://doi.org/10.1061/JHEND8.HYENG-13500>

## Electronic supplementary materials

Sections S1–S5

## 中文概要

**题目:** 高桩码头泥沙输运特性及减淤方法: 物理模型与现场试验研究

**作者:** 杨皓钧<sup>1,2</sup>, 高洋洋<sup>1,3</sup>, 王立忠<sup>1,3</sup>

**机构:** <sup>1</sup>浙江大学, 海洋学院, 中国杭州, 310058; <sup>2</sup>台州职业技术学院, 建筑工程学院, 中国台州, 318000; <sup>3</sup>浙江大学, 海南研究院, 中国三亚, 572025

**目的:** 高桩码头在复杂水沙环境下出现了严重的后方回淤问题。本文旨在探讨真实海洋环境下(潮汐流速、流向, 泥沙浓度, 地形等)对高桩码头周围的水沙运动特性及回淤机理, 并提

出绿色环保的减淤方法。

**创新点:** 1. 基于现场观测、大型物理模型港池试验, 探明了高桩码头的回淤机制; 2. 开展工程现场原位试验, 提出了一种绿色环保的减淤方法。

**方法:** 1. 通过现场观测和物理模型试验, 分析了高桩码头后方水沙运动与地形变化特征, 揭示了潮流、地形和桩群对淤积过程具有重要影响(图 13、图 15); 2. 通过物理模型模拟和现场验证, 提出了利用丁坝改善局部流场、减轻码头后方淤积的方法, 验证了该方法的可行性和有效性(图 18, 图 21)。

**结论:** 1. 高桩码头后方的泥沙淤积过程受潮流条件、地形特征和桩群阻力等因素共同影响; 2. 运用导流堤减淤方法对码头后方局部流场进行调控后, 淤积程度明显减轻。

**关键词:** 高桩码头; 现场试验; 泥沙输运; 大型物理模型试验; 导流堤